Serot *et al.* (9) and the calculations of Glendenning *et al.* (5), (GWM:neutrons) predict lower pressures. The uncertainty in the pressure due to the asymmetry term widens the range of possible EOSs that may be consistent with the experimental data. For this purpose, it is important to obtain experimental constraints on the asymmetry term (39–41) (see SOM text) and to complement them with improved constraints on the EOS of symmetric nuclear matter.

We have analyzed the flow of matter in nuclear collisions to determine the pressures attained at densities ranging from two to five times the saturation density of nuclear matter. We obtained constraints on the EOS of symmetric nuclear matter that rule out very repulsive EOSs from relativistic mean field theory and very soft EOSs with a strong phase transition at densities $\rho < 3\,\rho_0$, but not a softening of the EOS due to a transformation to quark matter at higher densities. Investigations of the asymmetry term of the EOS are important to complement our constraints on the symmetric nuclear matter EOS. Both measurements relevant to the asymmetry term and improved constraints on the EOS for symmetric matter appear feasible; they can provide the experimental basis for constraining the properties of dense neutron-rich matter and dense astrophysical objects such as neutron stars.

References and Notes

1. J. M. Lattimer, M. Prakash, *Astrophys. J.* **550**, 426 (2001).
2. H. A. Bethe, *Rev. Mod. Phys.* **62**, 801 (1990).
3. A. Akmal, V. R. Pandharipande, D. G. Ravenhall, *Phys. Rev. C* **58**, 1804 (1998).
4. M. Prakash, T. L. Ainsworth, J. M. Lattimer, *Phys. Rev. Lett.* **61**, 2518 (1988).
5. N. K. Glendenning, F. Weber, S. A. Moszkowski, *Phys. Rev. C* **45**, 844 (1992).
6. G. A. Lalazissis, J. König, P. Ring, *Phys. Rev. C* **55**, 540 (1997).
7. S. Typel, H. H. Wolter, *Nucl. Phys. A* **656**, 331 (1999).
8. R. B. Wiringa, V. Fiks, A. Fabrocini, *Phys. Rev. C* **38**, 1010 (1988).
9. H. Muller, B. D. Serot, *Nucl. Phys. A* **606**, 508 (1996).
10. H. Stocker, W. Greiner, *Phys. Rep.* **137**, 277 (1986).
11. W. Reisdorf, H. G. Ritter, *Annu. Rev. Nucl. Part. Sci.* **47**, 663 (1997).
12. K. G. R. Doss *et al.*, *Phys. Rev. Lett.* **57**, 302 (1986).
13. H. A. Gustafsson *et al.*, *Mod. Phys. Lett. A* **3**, 1323 (1988).
14. M. D. Partlan *et al.*, *Phys. Rev. Lett.* **75**, 2100 (1995).
15. J. Barrette *et al.*, *Phys. Rev. C* **56**, 3254 (1997).
16. H. Liu *et al.*, *Phys. Rev. Lett.* **84**, 5488 (2000).
17. H. H. Gutbrod *et al.*, *Phys. Lett. B* **216**, 267 (1989).
18. C. Pinkenburg *et al.*, *Phys. Rev. Lett.* **83** 1295 (1999).
19. P. Braun-Munzinger, J. Stachel, *Nucl. Phys. A* **638**, 3c (1998).
20. G. Bertsch, S. Das Gupta, *Phys. Rep.* **160**, 189 (1988).
21. Q. Pan, P. Danielewicz, *Phys. Rev. Lett.* **70**, 2062 (1993).
22. J. Zhang, S. Das Gupta, C. Gale, *Phys. Rev. C* **50**, 1617 (1994).
23. B.-A. Li, C. M. Ko, *Phys. Rev. C* **58**, 1382 (1998).
24. P. Danielewicz, *Phys. Rev. C* **51**, 716 (1995).
25. H. Sorge, *Phys. Rev. Lett.* **78**, 2309 (1997).
26. P. K. Sahu, W. Cassing, U. Mosel, A. Ohnishi, *Nucl. Phys. A* **672**, 376 (2000).
27. C. Fuchs, A. Faessler, E. Zabrodin, Y.-M. Zheng, *Phys. Rev. Lett.* **86**, 1974 (2001).
28. P. Danielewicz, *Nucl. Phys. A* **673**, 375 (2000).
29. G. D. Westfall *et al.*, *Phys. Rev. Lett.* **71**, 1986 (1993).
30. D. Brill *et al.*, *Zeit. Phys. A* **355**, 61 (1996).
31. P. Danielewicz, G. Odyniec, *Phys. Lett. B* **157**, 146 (1985).
32. P. Danielewicz, *Acta. Phys. Pol. B* **33**, 45 (2002).
33. J. Aichelin, A. Rosenhauer, G. Peilert, H. Stoecker, W. Greiner, *Phys. Rev. Lett.* **58**, 1926 (1987).
34. C. Gale, G. Bertsch, S. Das Gupta, *Phys. Rev. C* **35**, 1666 (1987).
35. The rapidity is defined by $y = \frac{1}{2}\ln\left(\frac{E + p_z c}{E - p_z c}\right)$, where c is the speed of light, is the momentum component parallel to the beam, and E is the total energy of the particle (including rest mass).
36. J.-Y. Ollitrault, *Phys. Rev. D* **46**, 229 (1992).
37. J. Badro *et al.*, *Phys. Rev. Lett.* **83**, 4101 (1999).
38. J. Boguta, *Phys. Lett. B* **109**, 251 (1982).
39. B.-A. Li, *Phys. Rev. Lett.* **85**, 4221 (2000).
40. M. Colonna, M. Di Toro, G. Fabbri, S. Maccarone, *Phys. Rev. C* **57**, 1410 (1998).
41. M. B. Tsang *et al.*, *Phys. Rev. Lett.* **86**, 5023 (2001).

42. Supported by NSF and the U.S. Department of Energy.

Supporting Online Material
www.sciencemag.org/cgi/content/full/1078070/DC1
SOM Text
References
Fig. S1

4 September 2002; accepted 22 October 2002
Published online 31 October 2002;
10.1126/science.1078070
Include this information when citing this paper.

Electron Acceleration by a Wake Field Forced by an Intense Ultrashort Laser Pulse

V. Malka,[1*] S. Fritzler,[1] E. Lefebvre,[2] M.-M. Aleonard,[3] F. Burgy,[1] J.-P. Chambaret,[1] J.-F. Chemin,[3] K. Krushelnick,[4] G. Malka,[3] S. P. D. Mangles,[4] Z. Najmudin,[4] M. Pittman,[1] J.-P. Rousseau,[1] J.-N. Scheurer,[3] B. Walton,[4] A. E. Dangor[4]

Plasmas are an attractive medium for the next generation of particle accelerators because they can support electric fields greater than several hundred gigavolts per meter. These accelerating fields are generated by relativistic plasma waves—space-charge oscillations—that can be excited when a high-intensity laser propagates through a plasma. Large currents of background electrons can then be trapped and subsequently accelerated by these relativistic waves. In the forced laser wake field regime, where the laser pulse length is of the order of the plasma wavelength, we show that a gain in maximum electron energy of up to 200 megaelectronvolts can be achieved, along with an improvement in the quality of the ultrashort electron beam.

The exploration of the fundamental nature of matter is the central quest of high-energy physics. In particular, collisions of particles at energies above 10^{11} eV are required to test some of the proposed grand unification theories, which may be able to describe all of the forces of nature. Consequently, efficient particle accelerators are essential for continuing progress in this field. At the present time, radio frequency cavities are used as accelerators. However, the technological limit of such devices is beginning to be approached, because the accelerating electric fields must be less than 55 MV/m to avoid material breakdown. To reach higher energies with reasonably sized facilities, a new and more efficient method of particle acceleration is required.

Mechanisms of laser-plasma acceleration. One possible alternative has been demonstrated in a number of proof-of-principle experiments over the past few years. In these experiments, high-amplitude relativistic plasma waves (RPWs) excited during laser-plasma interactions (1–4) have been used to accelerate electrons beyond 100 MeV. In the self-modulated laser wake field (SMLWF) regime, the laser pulse length $c\tau$ (where c is the speed of light and τ is the pulse duration) must be longer (5, 6) than the plasma wavelength λ_p. Because even for small-amplitude plasma waves the index of refraction is no longer constant but oscillates periodically, the laser pulse envelope becomes modulated at λ_p. This modulated beam in turn resonantly drives the amplification of the plasma wave. As a signature of this interaction, the transmitted laser spectrum exhibits forward Raman scattered satellites at frequencies of $(\omega_0 \pm n \cdot \omega_p)$, where ω_0 and ω_p are the laser and the plasma frequencies, respectively, and

[1]Laboratoire d'Optique Appliquée, École Nationale Supérieure des Techniques Avancées, École Polytechnique, CNRS, UMR 7639, 91761 Palaiseau, France. [2]Département de Physique Théorique et Appliquée, CEA/DAM Ile-de-France, BP 12, 91680 Bruyères-le-Châtel, France. [3]Centre d'Etudes Nucléaires Bordeaux Gradignan, IN2P3-Université de Bordeaux I, 33175 Gradignan, France. [4]Blackett Laboratory, Imperial College of Science, Technology, and Medicine, London SW7 2BZ, UK.

*To whom correspondence should be addressed. E-mail: victor.malka@ensta.fr

n is an integer corresponding to satellite order. Driven by the SMLWF instability (5–8), the electron density modulations in these plasma waves can reach a few tens of percent (9–13), which corresponds to electric fields on the order of 100 GV/m. The energetic electrons observed were generated in the plasma itself, initially being trapped in the plasma wave and then accelerated to high energy.

However, this mechanism is not possible if the laser pulse length is about the plasma wavelength. Nonetheless, electron trapping and acceleration can still be obtained as a result of the impulsive generation of a plasma wave and its breaking, in what we term the forced laser wake field (FLWF) regime. In this regime, the laser pulse is compressed by group velocity dispersion (14–16). The front of the pulse pushes electrons forward while the rear propagates in the density depression of the RPW. Consequently, the back of the pulse propagates faster than its front, compressing it to an optical shock. The resulting amplification of the ultrashort pulse, in particular the formation of an extremely sharp leading edge, can drive an RPW beyond its wavebreaking limit. In this case, there can be no spectral cascading of laser energy, and the only signature in the transmitted laser spectra will be a broadening of the driver laser frequency bandwidth.

The mechanics of the FLWF accelerator render it a superior electron source to the SMLWF accelerator in many respects. Because in the SMLWF the growth of the plasma wave is amplified from an initial small-amplitude seed, which itself depends on instabilities for its creation, the plasma wave characteristics can vary greatly from shot to shot (17). This is not the case for the FLWF regime. The lack of instabilities in the interaction also results in a lower plasma temperature. This is important because it means that the plasma wave amplitude can reach a much higher value, approaching the cold wavebreaking limit (18), $E_{WB} = \sqrt{2}\,(\gamma_p - 1)^{1/2}E_0$, where $E_0 = m_e c\omega_p/e$, e is the charge on the electron, m_e is the electron mass, and γ_p is the Lorentz factor associated with the plasma wave phase velocity, which for sufficiently underdense plasmas is approximately $(n_{cr}/n_e)^{1/2}$, the square root of the ratio of critical density to plasma density. In the SMLWF regime, the plasma wave amplitude is limited to the order of 10% of the ambient density by thermal loading of the plasma wave by hot background electrons (9–13), implying that the maximum energy to which electrons can be accelerated, $2\gamma_p^2\,(E_{max}/E_0)m_ec^2$, where E_{max} is the maximum electric field associated with the RPW, can be significantly higher in the FLWF. Another major advantage of the FLWF regime is its tolerance to initial plasma density, in contrast with the SMLWF and conventional laser wake field experiments. Through a combination of front-edge pulse sharpening, optical compression, and relativistic increase of the plasma wave wavelength, a large-amplitude plasma wave can be grown in the FLWF over a large range of initial plasma densities. Indeed, it is known that in the case of large-amplitude plasma wave creation by a laser pulse with a fast rise time, the back of the pulse plays little role in the plasma wave growth (19).

Also, as a result of the relativistic steepening of the plasma wave and optical compression of the laser, the accelerating plasma wave density spike, and thus most of the trapped and accelerated electrons, sit behind the laser pulse. This means that in the FLWF regime the effect of direct laser acceleration (DLA) is greatly reduced. DLA has been shown to be a possible accelerating mechanism in long-pulse high-intensity interactions (20), but it is associated with transverse momentum gain for the accelerated electrons, which can result in undesirable emittance growth. In the FLWF, the electrons interact primarily with the focusing and accelerating fields of the plasma wave, and this can result in greatly improved beam emittances.

Here, we report the first experimental evidence for the production of a beam of relativistic electrons due to wavebreaking in a short-pulse laser wake field experiment. The detection of electrons accelerated up to a maximum beyond 200 MeV in a well-collimated beam, and the relative insensitivity of this interaction to the initial plasma density, indicate that this acceleration is due to a FLWF mechanism. We also note that the measured emittance of the high-energy electrons is small, comparable to those found in present-day accelerator physics, and its generation using only a modestly sized laser system makes this scheme attractive as a source of relativistic electrons for many applications.

Experimental setup. The experiment was performed with a titanium-doped sapphire (Ti:Sa) laser (21) operating at 10 Hz and a wavelength λ_L of 820 nm in chirped-pulse amplification mode (22). The laser delivered energies up to 1 J on target in 30-fs full width at half-maximum (FWHM) pulses, with a linear polarization. The laser beam was focused with an f/18 off-axis parabolic mirror onto the edge of a supersonic helium gas jet (diameter 3 mm) to avoid refraction induced by ionization processes (23) (Fig. 1). The neutral-density profile jet was characterized by interferometry (24) and found to be uniform. The laser distribution at full energy in the focal plane was a Gaussian with a waist w_0 of 18 μm containing 50% of the total laser energy. This produces vacuum-focused intensities I_L on the order of 3×10^{18} W/cm^2, for which the corresponding normalized vector potential $a_0 = eA/m_0c^2$ is 1.2. The plasma period was chosen to vary between 25 and 14 fs by selecting initial electron densities between 2×10^{19} and 6×10^{19} cm^{-3}, which was achieved by changing the backing pressure on the gas jet.

Electron beam measurements. The characterization of the electron beam was performed with an electron spectrometer, integrating current transformer (ICT), radiochromic film, and nuclear activation techniques. A typical electron beam spectrum obtained at a plasma density of 2.5×10^{19} cm^{-3} is shown in Fig. 2. The total charge of the electron beam was measured to be about 5 nC, as determined with an ICT 10 cm in diameter, installed 20 cm behind the gas jet nozzle. Subsequently, the electron beam was collimated by an opening (internal diameter 1 cm) in a stainless steel piece (thickness 4 cm) at the entrance of an electron spectrometer, which gave a collection aperture of f/100. The electron spectrum was measured with five biased silicon-surfaced barrier detectors (SBDs) placed in the focal plane of the electron spectrometer. By changing the magnetic field in the spectrometer from 0 to 1.5 T, it is possible to measure electrons with energies from 0 to 217 MeV. The resulting spectrum is typical for those resulting from the wavebreaking of large-amplitude RPWs. In particular, although it is possible to fit a relativistic Maxwell-Jüttner distribution to the lower energy electrons [a longitudinal "effective temperature" of 18 (±1) MeV can be ascribed to

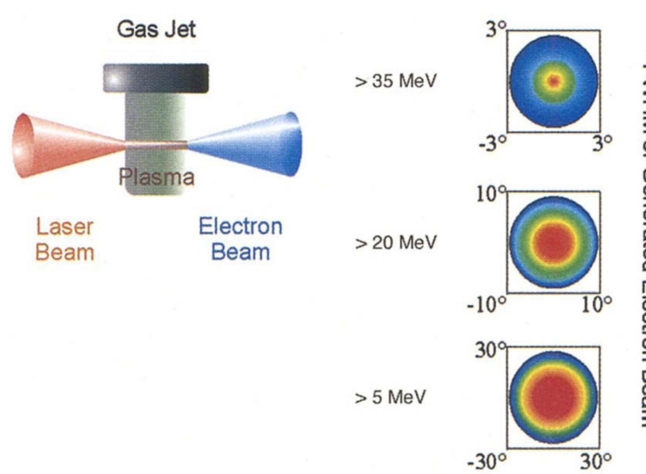

Fig. 1. Schematic of the experiment. A high-intensity laser is focused onto the sharp edge of a gas jet with a uniform density profile. In the FLWF regime, the generated plasma wave breaks and accelerates electrons. It is observed that the high-energy electrons are well collimated in the direction of propagation of the laser beam.

the electrons below 130 MeV in energy], this description is not adequate to describe the higher energy electrons. A significant number of electrons exist in a "hot tail" that extends beyond 200 MeV. The electron spectrum cannot be properly characterized without measuring these high-energy electrons. At this density, the cold wavebreaking limit E_{WB} is 3.8 E_0, and the maximum energy that an electron can gain in RPWs at this amplitude is slightly greater than 250 MeV. This indicates that the RPW excited by the short laser pulse does indeed reach an amplitude close to the cold wavebreaking limit, which is consistent with the absence of thermal effects in this regime. At a higher electron density (6×10^{19} cm^{-3}), similar spectra have been observed (charge and temperature), but without the hot tail. The plateau extending to 200 MeV has been observed for densities between 2.5×10^{19} and 4.7×10^{19} cm^{-3}.

The collimation of the electron beam is shown in Fig. 3 as a function of its energy. The high-energy part of the beam is observed to be well collimated, whereas the low-energy electrons are accelerated in a much broader cone in the forward direction. This observation has been verified by (γ, n) activation of ^{63}Cu and ^{12}C. In this case, the electron beam was first converted to bremsstrahlung by sending it through a tantalum piece 2 mm thick. The resulting γ-spectrum can be correlated with the initial electron spectrum by simulations with the Monte Carlo code GEANT. To trigger (γ, n) nuclear reactions in ^{63}Cu and ^{12}C, the incident photon energy must be above the threshold energies for these reactions, which are 10 and 18 MeV, respectively. Consequently, this diagnostic is solely sensitive to the higher energy part of the spectrum (*23*). The angular distribution of bremsstrahlung is obtained from measurements of the relative radioactivity of a number of targets, with dimensions 4 mm by 10 mm by 10 mm, which were placed in a circle 22.5 mm behind the converter. Their β^+-decay was measured by standard coincidence techniques in which the simultaneous measurement of two counterpropagating 511-keV photons is taken to be due to the annihilation of the positron inside the activation target. Assuming a Gaussian angular distribution for the electrons and bremsstrahlung, which is supported by the data obtained with radiochromic film, the FWHM of the angular distribution was measured to be 16° (±1°) and 10° (±1°) for 10- and 18-MeV electrons, respectively, whereas for energies above 35 MeV it was strongly reduced to 5° (±1°). This indicates a low emittance for the energetic electrons, which has been confirmed by accurate measurements of the electron beam divergence over the entire beam envelope using "pepper pot" masks (*25, 26*). With this technique, the normalized vertical emittance $\varepsilon_{n,x}$ was found to be 2.7 (±0.9) π mm mrad for 55 (±2) MeV electrons. This is well below the emittance of most present-day linear accelerators and emphasizes the quality of this energetic electron beam.

Numerical modeling. As mentioned, the generation of a plasma wave in front of the leading edge of the laser pulse results in pulse compression, with a corresponding broadening of its spectrum. This was experimentally observed, as the FWHM of the transmitted laser pulse spectrum of initially 33 nm in vacuum was increased to 48 nm for shots at full energy and a plasma electron density of 2.7×10^{19} cm^{-3} (Fig. 4). However, this temporal pulse amplification of about 50% cannot by itself account for the growth to wavebreaking amplitude of the RPW, using the one-dimensional (1D) nonlinear growth rates for laser wake field interactions (*4, 19*). To understand the behavior of the FLWF, one must perform 3D computer simulations of the interaction, including all the processes that can affect the RPW. This is done using the 3D Particle-In-Cell (3D-PIC) code CALDER.

This code includes a "moving window" capability (i.e., the simulation box moves with the laser pulse), thus enabling simulations with realistic parameters to be carried out, such as a 15-μm focal waist and a plasma 1 mm in length at a density of 1.2% n_{cr}. This calculation features more than 6×10^8 electrons and as many ions moving through a mesh with 1.5×10^8 cells. It was run on 500 nodes of the TERA supercomputer at CEA/DIF (Commissariat à l'Energie Atomique, Direction Ile de France). The laser pulse is injected into the plasma as a 30-fs FWHM Gaussian pulse with a peak irradiance of 3.5×10^{18} W/cm^2. Strong transverse self-focusing takes place in less than 300 μm inside the plasma, resulting in an order-of-magnitude increase in the pulse intensity. The strong ponderomotive force of this "light bullet" pushes electrons out of its path, driving a

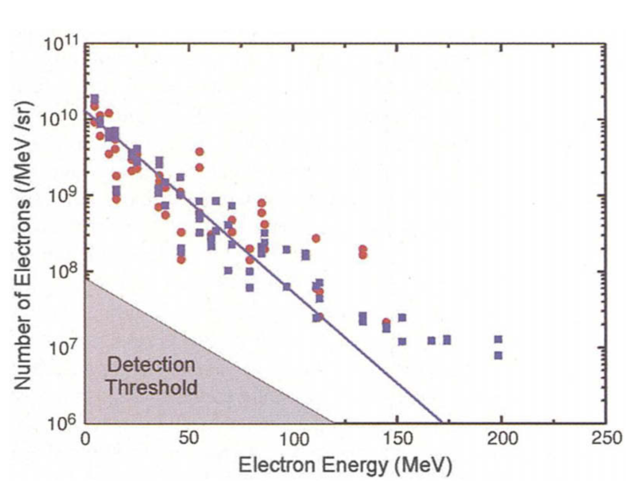

Fig. 2. Electron spectra for $n_e = 2.5 \times 10^{19}$ cm^{-3} (squares) and for $n_e = 6 \times 10^{19}$ cm^{-3} (circles). An effective longitudinal electron temperature of 18 MeV is obtained from an exponential fit, for electrons of less than 130 MeV (continuous line), for the lower density case. Several null tests were performed to ensure that the signal is due to electrons. First, sources of electronic noise in the data acquisition were suppressed. Second, the magnetic field was incrementally varied from 0 to 1.5 T for all the measurements, which changed the dispersion of the signal correspondingly. Because SBDs are also sensitive to bremsstrahlung, thick lead walls next to the collimator as well as around the detectors were set up to suppress stray γ-rays. Furthermore, because the spectrometer focuses the electron beam but obviously has no influence on the propagation of γ-rays, a clear distinction between the signal in and out of the focusing plane can be ascertained. Only signals with a signal-to-noise ratio of better than 25:1 were considered. The SBD signal is read out on an oscilloscope, so that only electron pulse signals synchronized to the laser pulse are taken into account. Finally, copper pieces 1 cm thick were installed directly in front of the SBDs. This changed the signals accordingly with the corresponding energy. All these factors allow us to have confidence in the obtained spectrum.

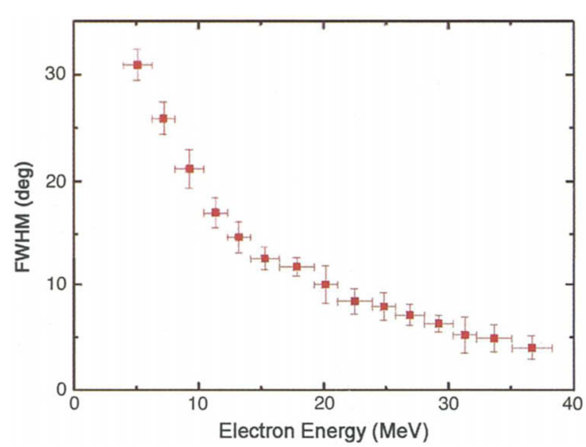

Fig. 3. FWHM of the angular distribution of the electron beam. The beam was visualized with a stack of radiochromic film (RCF) and electron energy was measured with the use of several 2-mm copper pieces. This stack was placed on the beam axis and shielded with aluminum wrapping to prevent illumination of the film by the laser. The traces on the film show the collimation of the electrons as a function of energy, which was required to pass the single copper and RCF pieces. Multiple scattering of the electrons inside this stack and superposition of the individual signals have been corrected.

large plasma wave in the wake of the pulse. After 210 μm, the electron density modulation and wake field have a relatively regular structure, with a maximum electric field of 1 $m_e c\omega_p/e$, or 430 GV/m (Fig. 5, A and B). This is a factor of 4 below the cold wavebreaking limit at this density. Some electrons have already been accelerated in this field to a maximum energy of 20 MeV. In the next 350 μm of propagation, the plasma wake and electron density evolve markedly. A large concentration of electrons is observed on axis, one-half plasma period behind the laser pulse, resulting in a density increase much larger than the background plasma density, $\delta n/n \gg 1$. The wake field amplitude grows close to the cold wavebreaking limit, reaching 3.2 $m_e c\omega_p/e$, or close to 1.4 TV/m (Fig. 5, C and D). The maximum electron energy rapidly increases, reaching 235 MeV after 560 μm of propagation in the plasma. Most of the accelerated electrons are located between 550 and 560 μm, in the density dip created by the pulse. The electron spectrum does not evolve substantially later on. The guided pulse propagation is sustained until the end of the simulation, at 900 μm, but the plasma wave loses some of its coherence and its amplitude is reduced. Half of the incident laser energy is transmitted through the first 900 μm of plasma. The energy distribution of electrons along the laser direction at this point (Fig. 6) is essentially identical to the spectrum at 560 μm. Counting all the particles above 1.25 MeV, we find a beam charge of 0.6 nC, an average electron energy of 11 MeV, and a total beam energy of 6.4 mJ (i.e., slightly more than 1% of the incident laser energy). The difference between the measured and computed beam charge reflects the low-energy electron contribution to the ICT measurement. Interestingly, the most energetic electrons are found to have a greater relative transverse component of their momenta. This is because, as they "outrun" the RPW, they are no longer influenced by its focusing effect, and so can gain transverse momentum from radial electrostatic and electromagnetic fields.

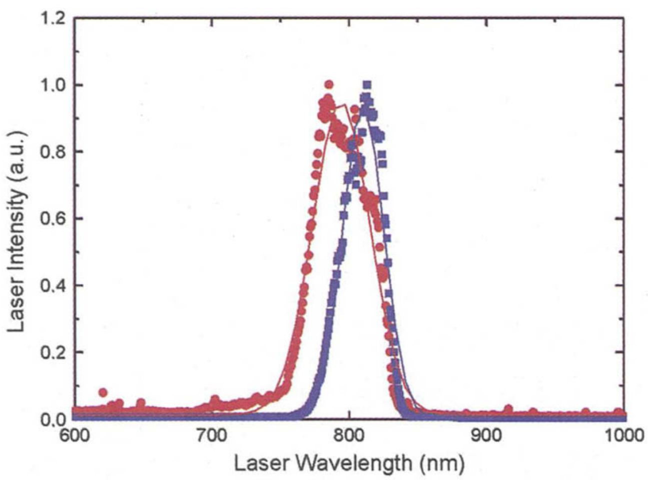

Fig. 4. Transmitted laser intensity as a function of wavelength in vacuum (squares) and in the plasma (circles). These spectra were acquired with a high-dynamic 18-bit charge-coupled device camera and are normalized. Their FWHM is obtained from a Gaussian fit and reveals the initial pulse spectrum to be 33 nm, whereas the plasma-distorted pulse is 48 nm. Note that no laser energy cascades to satellite frequencies.

Finally, it is noteworthy that although 2D simulations qualitatively show the same phenomena, they fail to correctly describe the self-focusing of the laser pulse and the maximum electron energy. All attempts to model this experiment with 2D simulations show a deficit of more than 50 MeV in the maximum electron energy, which was experimentally observed to be greater than 200 MeV. Consistent with other results (*16*), this 3D simulation clearly indicates that RPWs can be efficiently driven to wavebreaking in a regime where the pulse length is of the order of the plasma period, even though the resonance condition for classical wake field acceleration is not met.

Concluding remarks. It has been shown that focusing a 30-fs, 30-TW laser beam onto a gas jet generates a reproducible, bright, energetic, collimated, ultrashort electron beam. This source may become an interesting tool for many applications in physics as well as chemistry and biology. Because the high-energy electrons are well collimated, one can conceivably select a specific energy from the broad spectrum for use as an injector for a conventional accelerator. The short duration of

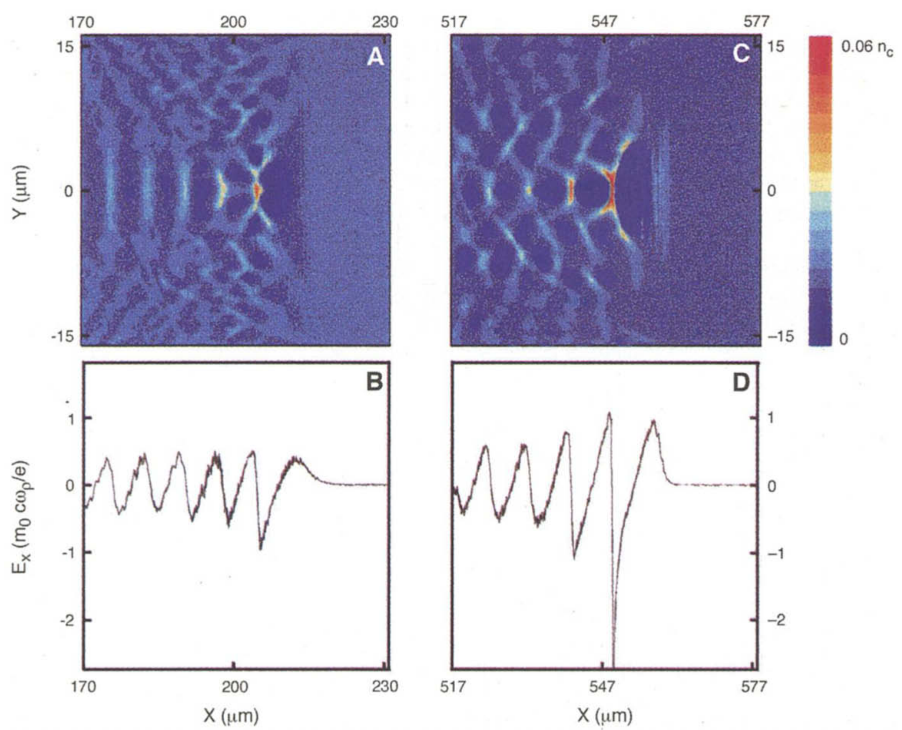

Fig. 5. Electron density cuts along the $z = 0$ plane and RPW electric fields along the laser axis after propagation through 210 μm (**A** and **B**) and 560 μm (**C** and **D**). In (C), the density scale has been truncated to 0.06 n_{cr} (i.e., five times the background density). In (D), the on-axis electric field of the RPW almost reaches the wavebreaking value of 4 $m_e c\omega_p/e$.

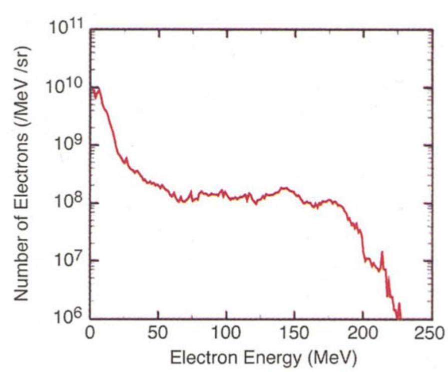

Fig. 6. Calculated electron energy distribution after propagating 900 μm through the plasma. This spectrum is measured inside a 2° half-angle cone along the laser axis, which is the angular resolution of the code diagnostic. The total charge of the electron beam for electrons above 1.25 MeV is 0.6 nC.

this high-current electron beam generated by an ultrashort laser pulse means that flashes of γ-rays can be generated (*27*), which can be shorter in duration and thus brighter than those generated by electron beams from contemporary linear accelerators. Similarly, in chemistry, radiolysis and fast kinetic reactions induced by high bunch charge electron beams can be investigated with a time resolution better than 100 fs. Also, focusing a second terawatt laser on the electron beam by a pump-probe technique can generate a short and bright x-ray pulse, which is of interest for the study of fast phenomena in biology and crystallography. A final but important consideration is the rapid evolution of the type of "table-top terawatt laser systems" used in this study. Today these cost about 1 million euros and operate at 10 Hz. It is expected that their repetition rate will be increased in the near future to the kHz regime while their cost will be reduced. Consequently, the availability of such laser-plasma accelerators for universities and small laboratories promises to open up a broad spectrum of research in the near future.

References and Notes

1. T. Tajima, J. Dawson, *Phys. Rev. Lett.* **43**, 267 (1979).
2. A. Modena *et al.*, *Nature* **377**, 606 (1995).
3. M. I. Santala *et al.*, *Phys. Rev. Lett.* **86**, 1227 (2001).
4. E. Esarey, P. Sprangle, J. Krall, A. Ting, *IEEE Trans. Plasma Sci.* **24**, 252 (1996), and references therein.
5. E. Esarey, J. Krall, P. Sprangle, *Phys. Rev. Lett.* **72**, 2887 (1994).
6. N. E. Andreev, L. M. Gorbunov, V. I. Kirsanov, A. A. Pogosova, R. R. Ramazashvili, *JETP Lett.* **55**, 571 (1992).
7. T. M. Antonsen, P. Mora, *Phys. Rev. Lett.* **69**, 2204 (1992).
8. P. Sprangle, E. Esarey, J. Krall, G. Joyce, *Phys. Rev. Lett.* **69**, 2200 (1992).
9. C. E. Clayton *et al.*, *Phys. Rev. Lett.* **81**, 100 (1998).
10. A. Ting *et al.*, *Phys. Rev. Lett.* **77**, 5377 (1996).
11. S. P. LeBlanc *et al.*, *Phys. Rev. Lett.* **77**, 5381 (1996).
12. D. Gordon *et al.*, *Phys. Rev. Lett.* **80**, 10 (1998).
13. C. I. Moore *et al.*, *Phys. Rev. Lett.* **79**, 3909 (1997).
14. C. D. Decker, W. B. Mori, K. C. Tzeng, T. Katsouleas, *Phys. Plasmas* **3**, 2047 (1996).
15. W. P. Leemans *et al.*, *IEEE Trans. Plasma Sci.* **24**, 331 (1996).
16. A. Pukhov, J. Meyer-ter-Vehn, *Appl. Phys. B* **74**, 355 (2002).
17. Z. Najmudin *et al.*, *IEEE Trans. Plasma Sci.* **28**, 1057 (2000).
18. A. I. Akhiezer, R. V. Polovin, *Sov. Phys. JETP* **3**, 696 (1956).
19. S. V. Bulanov, V. I. Kirsanov, A. S. Sakharov, *Sov. Phys. JETP* **50**, 198 (1989).
20. A. Pukhov, Z.-M. Zheng, J. Meyer-ter-Vehn, *Phys. Plasmas* **6**, 2847 (1998).
21. M. Pittman *et al.*, *Appl. Phys. B* **74**, 529 (2002).
22. D. Strickland, G. Mourou, *Opt. Commun.* **56**, 219 (1985).
23. C. D. Decker, D. C. Eder, R. A. London, *Phys. Plasmas* **3**, 414 (1996).
24. V. Malka *et al.*, *Rev. Sci. Instrum.* **71**, 2329 (2000).
25. Y. Yamazaki, T. Kurihara, H. Kobayashi, I. Sato, A. Asami, *Nucl. Instrum. Methods A* **322**, 139 (1992).
26. S. Fritzler *et al.*, in preparation.
27. R. D. Edwards *et al.*, *Appl. Phys. Lett.* **80**, 2129 (2002).

28. This work was partially supported by the EU Access to Research Infrastructure under LOA Contract HPRI-1999-CT-00086.

30 July 2002; accepted 15 October 2002

REPORTS

Fluorometric Detection of Enzyme Activity with Synthetic Supramolecular Pores

Gopal Das, Pinaki Talukdar, Stefan Matile*

The reversible blockage of synthetic pores formed by rigid-rod β barrels, either by substrates or products, was used to sense a variety of enzymatic reactions in high-throughput format with "naked-eye" fluorescent detection. Improvement of sensor sensitivity beyond three orders of magnitude by straightforward internal mutations underscores the functional plasticity of rigid-rod β barrels. Such detectors of enzyme activity with the aforementioned characteristics are needed in areas as diverse as proteomics and environmentally benign organic synthesis.

A promising approach for analyzing biological molecules is to harness the selectivity of transmembrane pores. Such approaches usually require the engineering of natural (*1, 2*) or artificial (*3–9*) pores, so that they are selectively blocked by an analyte of interest, and a detection scheme, often the determination of ion currents.

Rather than rely on the complexities of measuring ion currents to detect an analyte of interest, we devised a fluorescent dye method to determine the progress of enzymatic reactions that convert good pore blockers into poor ones (or poor blockers into good ones). Methods that allow enzymatic activity to be screened rapidly are needed both for developing new reaction routes, such as in carbohydrate synthesis (*10–12*), and for identifying enzyme inhibitors for pharmaceutical use (*13, 14*). Many enzymes of interest are phosphatases that convert a substrate, such as adenosine triphosphate (ATP), into smaller molecules, such as adenosine monophosphate (AMP) or inorganic phosphate (P_i) (*13, 15*).

We designed several pores that are blocked to a much larger extent by these larger substrates [as reflected in their dissociation constant (K_D)] than by the smaller reaction products. These pores were introduced into large unilamellar vesicles (LUVs) containing a fluorescent dye at concentrations high enough that emission is self-quenched. The extent of conversion of the substrate of interest (i.e., ATP) will cause differential rates of leakage of the dye from the vesicles, which will be reflected in an increase in fluorescence from the vesicles as self-quenching is diminished.

We used engineered rigid-rod β barrels as the pores. We have previously demonstrated the self-assembly of these synthetic barrel-stave supramolecules (*6–9*). The key element

Department of Organic Chemistry, University of Geneva, CH-1211 Geneva, Switzerland.

*To whom correspondence should be addressed. E-mail: stefan.matile@chiorg.unige.ch

Table 1. Binding of substrates and products to synthetic supramolecular pores. Abbreviations and materials can be found in Fig. 2 and (*18*). Dissociation constants (K_D) are given in micromolar concentration (*17*). ND, not determined.

Entry	Enzyme	Pore	Substrates	K_D (μM)	Products	K_D (μM)
1	Apyrase	$\mathbf{1} \supset Mg^{2+}{}_n$	ATP	6,700*	AMP†	20,400*
2	Apyrase	**2**	ATP	2	AMP†	66
3	Apyrase	$\mathbf{1} \supset Mg^{2+}{}_n$	TPP	10,000*	Thiamine†	>240,000*
4	Apyrase	**2**	TPP	440	Thiamine†	ND
5	Aldolase‡	$\mathbf{1} \supset Mg^{2+}{}_n$	FDP	21,800*	DHAP‡	>150,000
6	Aldolase‡	**2**	FDP	220	DHAP‡	>2,500
7	Alkaline phosphatase	**2**	UDP	1,175	U†	>75,000
8	Galactosyltransferase	**2**	UDPGal	>75,000	UDP	1,175
			GlcNAc	>50,000	Galβ1→GlcNAc	>50,000

*Data from (*8*). †P_i [$H_nPO_4^{-(3-n)}$]: K_D ($\mathbf{1} \supset Mg^{2+}{}_n$) = 66.6 mM (*8*), K_D (**2**) = 12.0 mM. ‡Glyceraldehyde 3-phosphate was converted to dihydroxyacetone phosphate (DHAP) by TIM.